Inorganic Chemistry

Article

pubs.acs.org/IC

Linking ^{31}P Magnetic Shielding Tensors to Crystal Structures: Experimental and Theoretical Studies on Metal(II) Aminotris(methylenephosphonates)

Johannes Weber,[†] Gisbert Grossmann,[‡] Konstantinos D. Demadis,*[,§] Nikos Daskalakis,[§] Erica Brendler,[⊥] Martin Mangstl,[†] and Jörn Schmedt auf der Günne*[,†]

[†]Department of Chemistry, Ludwig-Maximilians-Universität, D-81377 Munich, Germany

[‡]Department of Chemistry, Technische Universität Dresden, D-01062 Dresden, Germany

[§]Crystal Engineering, Growth and Design Laboratory, Department of Chemistry, University of Crete, P.O. Box 2208, Voutes Campus, Heraklion GR-71003, Crete, Greece

[⊥]Fakultät für Chemie und Physik, TU Bergakademie Freiberg, Leipziger Strasse 29, D-09599 Freiberg, Germany

Supporting Information

ABSTRACT: The ^{31}P chemical shift tensor of the phosphonate group $[RC\text{-}PO_2(OH)]^-$ is investigated with respect to its principal axis values and its orientation in a local coordinate system (LCS) defined from the P atom and the directly coordinated atoms. For this purpose, six crystalline metal aminotris(methylenephosphonates), $MAMP{\cdot}xH_2O$ with M = Zn, Mg, Ca, Sr, Ba, and (2Na) and x = 3, 3, 4.5, 0, 0, and 1.5, respectively, were synthesized and identified by diffraction methods. The crystal structure of water-free BaAMP is described here for the first time. The principal components of the ^{31}P shift tensor were determined from powders by magic-angle-spinning NMR. Peak assignments and orientations of the chemical shift tensors were established by quantum-chemical calculations from first principles using the extended embedded ion method. Structure optimizations of the H-atom positions were necessary to obtain the chemical shift tensors reliably. We show that the ^{31}P tensor orientation can be predicted within certain error limits from a well-chosen LCS, which reflects the pseudosymmetry of the phosphonate environment.

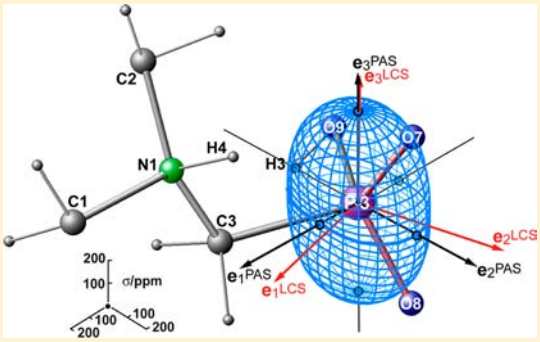

INTRODUCTION

Phosphonates occur in numerous functional materials, like porous materials,[1,2] ion exchangers,[3,4] limescale inhibitors,[5,6] catalysts,[7] and medical applications, e.g., treatment of osteoporosis and bone cancer.[8] While most drugs are based on geminal bisphosphonates ($R\text{-}CH(PO_3H)_2$), biological activity has also been reported for monophosphonates ($R\text{-}CH_2PO_3H$).[9] Glyphosate ($HO_2CCH_2NH_2CH_2PO_3H$) is the most used systemic herbicide (active ingredient in Roundup) worldwide with consumptions of about 600000 tons/year.[10] Moreover, monophosphonates occur naturally, e.g., as phosphonolipids[11] in cell membranes of certain microorganisms, marine animals, and plants or as (2-aminoethyl)-phosphonate ($H_3NCH_2CH_2PO_3H$) in the human body.[12]

To understand interactions, functionality, and degradation of phosphonates in biological systems on a molecular level, analytical methods with resolution on an atomic scale are required. Solid-state magic-angle-spinning (MAS) ^{31}P NMR spectra can provide valuable information for structure elucidation. Especially, the principal axis values δ_{11}, δ_{22}, and δ_{33} and the chemical shift tensor orientation, i.e., collection of the three orthogonal principal axes $\{\mathbf{e}_1^{PAS}, \mathbf{e}_2^{PAS}, \text{and } \mathbf{e}_3^{PAS}\}$, of the chemical shift tensor $\overleftrightarrow{\delta}^{31P}$ can be useful quantities because they are related to the local configuration, conformation, and coordination of the phosphonate unit. While principal axis values have been frequently used to derive structural information,[13] studies on shift tensor orientations on phosphonates are relatively rare.[14] This is astonishing because shift tensor orientations of analogous thiophosphonates[15] and phosphates[16] have gained considerable interest, especially with respect to structure elucidation, dynamics, and functionality of phospholipids.[17]

All structural information derived from experimental shift tensor orientations is based on the assumption that one can relate the tensor principal axis system (PAS) to a suitable local reference coordinate system (LCS). Before $\overleftrightarrow{\delta}^{31P}$ tensor orientations can be used for structural statements on noncrystalline systems, the characteristic $\overleftrightarrow{\delta}^{31P}$ orientation for a phosphonate unit needs to be established in a molecular frame and estimates for the variability of the tensor orientation have to be determined. This is best done for crystalline model

Received: June 8, 2012
Published: October 5, 2012

Table 1. Investigated *M*AMP Compounds

abbreviation	unit formula	reference, CCDC code
ZnAMP·3H_2O	Zn[$HN(CH_2PO_3H)_3$]·3H_2O	24, FIYGAW
MgAMP·3H_2O	Mg[$HN(CH_2PO_3H)_3$]·3H_2O	25, IDAJED
CaAMP·4.5H_2O	Ca[$HN(CH_2PO_3H)_3$]·4.5H_2O	26, BEKIBD02[a]
SrAMP	Sr[$HN(CH_2PO_3H)_3$]	25, IDAJIH
BaAMP	Ba[$HN(CH_2PO_3H)_3$]	this paper, entry no. 658991
(2Na)AMP·1.5H_2O	Na_2[$HN(CH_2PO_3H)_3$]·1.5H_2O	27, BEGPIM

[a]In the CCDC, the sum formula is erroneously described as CaAMP·3.5H_2O.

compounds where both the molecular structure and the $\overleftrightarrow{\delta}^{31P}$ tensor orientation can be determined by experimental or theoretical methods. Experimentally, tensor orientations are amenable by single-crystal NMR studies,[14a,16,18] which are cumbersome, however. Alternatively, full shielding tensor information can be calculated quantum chemically for solid matter with different approaches, which are typically classified in calculations under periodic boundary conditions or cluster calculations. The use of cluster calculations for the determination of ^{31}P shift tensors in phosphonates was already recognized in earlier works.[14b,19] In the present work, we use a recently proposed cluster method for calculations of crystals, the extended embedded ion method (*EEIM*).[20]

In this paper, we want to establish the ^{31}P shielding tensor orientation of phosphonates in a LCS, whose origin is centered at the P atom and whose basis vectors are derived in a systematic way from the nearest-neighboring atoms. To this end, we study both in experiment (by solid-state cross-polarization (CP) MAS $^{31}P\{^1H\}$ NMR of powdered crystals) and in theory a set of metal phosphonates, *M*AMP·*x*H_2O with *M* = Zn, Mg, Ca, Sr, Ba, and (2Na) and AMP = aminotris(methylenephosphonic acid)[21], all of which are zwitterionic in solution[22] and in the solid state[23] and possess monoprotonated phosphonate groups only. Despite the similarity in their covalent backbones, the compounds show a rich diversity in the (noncovalent) coordination of the phosphonate groups to the metal ions. Abbreviations, formulas, and references to the crystal structure of these compounds are given in Table 1. Experimental shift tensor principal axis values are used to validate the theoretical calculations. As a side effect, an assignment of the experimental NMR signals to crystallographic P sites is obtained, which is difficult to achieve otherwise for nuclei in a chemically similar environment.

EXPERIMENTAL SECTION

Materials. All water-soluble metal salts were commercial samples and were used without further purification. Aminotris(methylenephosphonic acid) (AMP; 50% w/w solution in water as acid) was from ThermPhos, Switzerland. Stock solutions of HCl and NaOH were used for pH adjustments.

Syntheses of *M*AMP·*x*H_2O. The compounds with *M* = Zn, Mg, Ca, Sr, and (2Na) and *x* = 3, 3, 4.5, 0, and 1.5, respectively, were prepared according to published procedures.[25,27] In general, the preparation is based on a reaction of water-soluble metal salts and AMP (in acid form) in a 1:1 molar ratio under ambient conditions and at pH < 1.5. The compounds were structurally characterized, and their compositions were ZnAMP·3H_2O,[24] MgAMP·3H_2O,[25] CaAMP·4.5H_2O,[26] SrAMP,[25] and (2Na)AMP·1.5H_2O.[27] The product of the reaction between Ba^{2+} and AMP^{2-} yielded a powder X-ray diffraction (XRD) pattern that did not coincide with the experimental powder pattern of BaAMP·H_2O reported before.[25] Therefore, we reinvestigated this reaction and solved the crystal structure of the product, which proved to be a new, *anhydrous* compound BaAMP.

Synthesis of BaAMP. A quantity of AMP (8.8 mL of a 50% w/w solution, 20 mmol) was added to 31.2 mL of deionized water. This solution had a pH of 0.67. Then, to this solution was added in small portions and under vigorous stirring 4.888 g of $BaCl_2·2H_2O$ (20 mmol). During this time, the solution pH dropped to 0.34. The clear colorless solution was handled in different ways: (i) It was placed under reflux conditions for 7 days, after which small colorless crystals formed at the bottom of the flask. The solution was then removed from the heating mantle and allowed to cool. The microcrystalline material was isolated by filtration, washed with deionized water, and air-dried. Yield: ≈70%. (ii) The solution was left several days at room temperature. (iii) The solution was placed in a fridge at 5 °C. Highly crystalline material started to form after ≈6 h. It was isolated by filtration, washed with deionized water, and air-dried. When the filtrate was again placed in the fridge, additional material was crystallized. Yield: ≈95%. The compositions of the three crystalline products prepared by methods i–iii were identical. Elemental analysis. Calcd (found) for $BaC_3H_{10}P_3O_9$ (BaAMP): C, 8.29 (8.14); H, 2.30 (2.43); N, 3.22 (3.39).

Instrumentation. The thermogravimetric analysis (TGA) apparatus was a 1100-Mettler TGA/SDTA 851-LF, with the carrier gas being either air or N_2 at a flow rate of 100 mL/min. Samples were heated from 298 to 1073 K, at a heating rate of 7 K/min in an aluminum crucible (volume 30 μL). The TGA curve of BaAMP is shown in Figure S1 in the Supporting Information (SI). No weight loss was observed for temperatures up to ≈673 K, which is a strong indication that the compound does not contain volatile H_2O molecules, a fact that is confirmed by its crystal structure discussed below. Above 673 K, a gradual weight loss occurred, which represents ligand decomposition, up to ≈973 K, where the final decomposition product ($Ba_2P_2O_7$) is formed and identified by powder XRD.

Powder XRD patterns were collected on a PANanalytical X'Pert Pro automated diffractometer or on a Huber G670. In Figure S2 in the SI, the experimental and simulated powder patterns are shown. The investigated single crystal and the *bulk* material of BaAMP have the same structure.

Single-Crystal X-ray Data Collection for BaAMP. XRD data were collected on a Bruker AXS SMART 1K CCD area detector with graphite-monochromated Mo Kα radiation at room temperature using the program *SMART-NT*[28] and processed by *SAINT-NT*.[29] Empirical absorption correction was applied by the program *SADABS*.[30] The structure was solved by direct methods and refined by full-matrix least-squares cycles on F^2. All non-H atoms were refined anisotropically. Methylene group H atoms were located from difference maps, while acid protons were geometrically positioned and left riding on their parent atoms during structure refinement. Crystallographic data for BaAMP are given in Table 2.

Solid-State ^{31}P NMR Measurements. Solid-state MAS ^{31}P NMR spectra of powdered samples were recorded on a Bruker AVANCE 400 WB spectrometer (162.02 MHz for ^{31}P) with a commercial MAS probe for 4 mm rotors. CP $^{31}P\{^1H\}$ NMR experiments were performed with a 50% ramp and high-power ^1H decoupling during data acquisition. The length of the 90° pulse was 2.8 μs, the contact time 5 ms, and the repetition delay 20 s. Calibration was done using AMP as the external standard with δ_P = 12.5 ppm relative to 85% H_3PO_4. Spectra were recorded at MAS frequencies of 4 or 5 kHz in order to extract principal axis values δ_{11}, δ_{22}, and δ_{33} of chemical shift tensors by analysis of the sideband intensities and at 10 kHz for direct

dx.doi.org/10.1021/ic301192y | *Inorg. Chem.* 2012, 51, 11466–11477

Table 2. Crystallographic Data for BaAMP

empirical formula	$C_3H_{10}NO_9P_3Ba$
fw	434.37
cryst color	colorless
cryst size (mm^3)	0.04 × 0.15 × 0.18
cryst system	triclinic
space group	$P\bar{1}$ (No. 2)
a (Å)	7.638(1)
b (Å)	8.483(1)
c (Å)	9.142(1)
α (deg)	101.766(3)
β (deg)	95.984(3)
γ (deg)	107.083(2)
V (Å^3)	545.7(2)
Z	2
temp (K)	293(2)
λ (Å)	0.71073
ρ (g/cm^3)	2.643
μ (cm^{-1})	4.117
$R(F_o)^a$	0.0298
$wR(F_o^2)^b$	0.0682

$^aR = \sum||F_o| - |F_c||/\sum|F_o|$. $^bwR = \{\sum[wR(F_o^2 - F_c^2)^2]/\sum[w(F_o^2)^2]\}^{1/2}$.

measurement of the isotropic chemical shift δ_{iso}. The δ_{ii} values (i = 1–3) were calculated using the program *WINMAS*,[31] which is based on the method of Herzfeld and Berger.[32] As seen in Figures S5–S10 in the SI, the simulated MAS NMR spectra based on the results of sideband intensity analysis agree well with the experimental ones. The data are reported following the convention $\delta_{11} \geq \delta_{22} \geq \delta_{33}$ and $\sigma_{11} \leq \sigma_{22} \leq \sigma_{33}$.[33]

COMPUTATIONAL DETAILS

Partial Structure Optimizations. The H-atom positions of experimental *M*AMP·xH$_2$O crystal structures (*M* = Mg, Ca, Sr, Ba, and Zn)[24−27] were optimized by quantum-chemical calculations under periodic boundary conditions, because XRD structures are inaccurate in this respect. The remaining fractional atomic coordinates and cell parameters as well as the unit cell symmetry were kept constant during optimization, with one exception as discussed in the next paragraph. For a better comparison of the *M*AMP structures, we relabeled the atomic sites. The P sites were labeled according to the torsion angles τ(Pi–C–N–H) ∈ [−180°, +180°] in the following order: $|\tau$(P2–C–N–H)| > $|\tau$(P1–C–N–H)| > $|\tau$(P3–C–N–H)|. The O sites within each phosphonate group were numbered in ascending order with increasing bond lengths d(P–Oi). Figure 1 shows the uniform labeling of the investigated *M*AMP units in detail using the example of SrAMP. The labels used in earlier literature and in this paper are juxtaposed in Tables S1–S5 in the SI.

The problem of partial occupancies of the three sites "H42a", "O42", and "H42b" (according to the labeling of the original CIF file) in CaAMP·4.5H$_2$O was solved by assuming a $P2_1$ (No. 4) symmetric superstructure in which the half-occupied sites from the initial $P2_1/n$ (No. 14) structure were split into sites with a regular occupation of 1 and "defect sites" with an occupation of 0. In addition to optimization of all of the H-atom positions, the O-atom positions on the occupied "O42" sites were optimized as well because a deviation of more than 0.06 Å is observed between published XRD data at 173 K[26] and at room temperature.[13d] Hence, the supercell may be termed as (CaAMP)$_2$·9H$_2$O because it contains two crystallographically different AMP units that, however, have identical molecular backbones. Further details on the $P2_1$ structure of (CaAMP)$_2$·9H$_2$O are given in Figures S13–S15 and Tables S3 and S8 in the SI.

For SrAMP, we performed two further calculations: (i) optimization of the fractional coordinates of all atomic sites (not just H) with constant cell parameters and symmetry and (ii) full relaxation of the fractional coordinates and cell parameters with fixed cell symmetry. The structures resulting from the different optimizations were used in the NMR calculations described in the next section.

Figure 1. Uniform labeling of SrAMP as the prototype for *M*AMP structures with *M* = Zn, Mg, Ca, Sr, and Ba. The two shortest terminal P–O$_{t/t'}$ bonds in each CPO$_3$ unit are highlighted in red.

All optimizations were performed with the *VASP* program[34] at the generalized gradient approximation (GGA) density functional theory (DFT) level using the PW91 functional.[35] The projector-augmented-wave (PAW) method was employed[36] with an energy cutoff of 500 eV for the plane-wave basis expansion. Optimized pseudopotentials for PW91/PAW (included in the *VASP* package) and default values for the expansion of angular momentum projection operators in the augmentation region were used. Automatic selection of k points was performed by the Monkhorst–Pack scheme.[37] The final calculations employed a 4 × 4 × 4 mesh. In single-point calculations with increasing mesh sizes (up to 8 × 8 × 8), this turned out to be sufficient for energies converged to 10^{-3} eV (=0.1 kJ/mol). The tetrahedron method with Blöchl's corrections[38] was used for Brillouin-zone integration.

Tight convergence criteria (`Precision=HIGH`) were used during the calculations. Structures were considered as converged when the change in the free energy between two subsequent structural relaxation steps was below 10^{-6} eV, the residual forces were converged to 5 × 10^{-3} eV/Å, and a subsequent run at the updated structure with updated plane-wave basis expansion did not change the energy by more than 10^{-4} eV. An energy-based convergence criterion was used in the self-consistent-field (SCF) procedure. The electronic wave function was considered as converged if the energy change in subsequent SCF cycles was below 10^{-7} eV.

NMR Calculations. Absolute magnetic shielding tensors $\vec{\sigma}$ were calculated with the *EEIM*, an embedded cluster approach in which the quantum cluster (QC; i.e., the quantum chemically treated region) is placed in an exact, self-consistent electrostatic crystal potential, which is obtained from *first principles*, i.e., without empirical parameters. For details on the *EEIM*, we refer to ref 20. A typical QC contained eight formula units, [*M*AMP·xH$_2$O]$_8$, where a central AMP^{2-} unit is surrounded by seven AMP^{2-} units, H$_2$O molecules, and an appropriate amount of counterions M^{2+} in order to take hydrogen bridge bonding and coordinative bonding of the central unit into account as well as to satisfy the charge-neutrality criterion (q^{QC} = 0).

The atoms surrounding the central AMP unit in the construction of [*M*AMP·xH$_2$O]$_8$ emerged rather naturally from a spherical shell expansion of 3.7 Å around the three central P sites, fragment completion, and filling of nearby M^{2+} sites (and H$_2$O where required) so that the relative frequencies of all atomic sites in the QC coincide with the relative frequencies in the unit cell. For comparison, we also performed calculations on smaller QCs, [*M*AMP·xH$_2$O]$_1$ (for the case of [SrAMP]$_1$, see Figure 1) and [AMP]$^{2-}$, where intermolecular

dx.doi.org/10.1021/ic301192y | Inorg. Chem. 2012, 51, 11466–11477

Table 3. Local Structure Information and Site Labeling of the Phosphonate Units in $M^{2+}[HN(CH_2PO_3H)_3]^{2-}$

	M^{2+}				
	Zn^{24}	Mg^{25}	Ca^{26}	Sr^{25}	Ba (this paper)
space group	$P2_1/c$	$P2_1/c$	$P2_1/n$	$P2_1/n$	$P\bar{1}$
asymmetric unit	$ZnAMP{\cdot}3H_2O$	$MgAMP{\cdot}3H_2O$	$CaAMP{\cdot}4.5H_2O$	SrAMP	BaAMP
coord no.[a] of M^{2+}	6 (3W)	6 (3W)	6 (1W)	7	9
Pi[b]	P1/P2/P3	P1/P2/P3	P1/P2/P3	P1/P2/P3	P1/P2/P3
d(Pi–O_t)/Å[c]	1.4999/1.4971/1.5039	1.5002/1.4978/1.5018	1.4943/1.5035/1.4931	1.4919/1.5000/1.4884	1.4845/1.4949/1.4869
d(Pi–$O_{t'}$)/Å	1.5202/1.5043/1.5096	1.5160/1.4983/1.5024	1.5102/1.5040/1.5035	1.5050/1.5091/1.4925	1.5123/1.5065/1.5123
d(Pi–O_b)/Å	1.5636/1.5699/1.5668	1.5636/1.5.697/1.5656	1.5684/1.5703/1.5802	1.5732/1.5651/1.5782	1.5747/1.5666/1.5699
d(Pi–C)/Å	1.8309/1.8256/1.8250	1.8292/1.8240/1.8253	1.8330/1.8347/1.8382	1.8296/1.8270/1.8268	1.8273/1.8150/1.8321
β(O_t–Pi–$O_{t'}$)/deg	115.0/115.6/115.0	115.2/115.9/115.5	116.1/114.5/118.3	114.8/112.8/120.6	117.2/117.5/113.7
$\lvert\tau$(Pi–C–N–H)$\rvert$/deg	55.2/172.0/46.9	54.8/168.5/43.9	63.9/172.3/41.7	58.3/171.6/46.6	43.7/169.1/32.9
connectivity of the PO_3H group to the M^{2+} ions					
O_t	0/1/1	0/1/1	1/1/1	1/2/1	1/2/1
$O_{t'}$	0/1/0	0/1/0	1/0/1	1/1/1	1/1/2
O_b	0/0/0	0/0/0	0/0/0	0/0/0	0/1/0

[a]In parentheses, the number of coordinated H_2O molecules. [b]For a better comparison of different *M*AMP crystal structures, the nonuniform labeling of atoms in previously published works was changed to a consistent labeling. Labels Pi (i = 1–3) for P atoms are chosen according to the following order of the torsion angles: $\lvert\tau$(P2–C–N–H)$\rvert$ > $\lvert\tau$(P1–C–N–H)$\rvert$ > $\lvert\tau$(P3–C–N–H)$\rvert$. The labels used in XRD and in this paper are juxtaposed in Tables S1–S5 in the SI. [c]O_t, $O_{t'}$, and O_b indicate the first, second, and third nearest neighbors to the respective P atom.

hydrogen bonds and most coordinative bonds are absent. The last QC is not charge-neutral and displays the default choice for the cheaper embedded ion method.[39] Further details on the cluster construction and the embedding charge field are given in the SI, Chapter 6.

A locally dense basis expansion was used, where Gaussian atomic basis functions (AOs) were assigned by means of a spherical shell expansion around a set of reference points $\{r_{ref,1}, r_{ref,2}, ..., r_{ref,k}\}$ (see ref 20 for details). In the present calculations, this set contained all atomic positions of the central AMP unit (k = 26). In the innermost shell (shell range r_1 = [0, 1.0] Å), a 6-311G(3df,3dp) basis set[40] was provided to the atoms. The 6-31G(d,p) basis set[41] was used in the second shell (typical shell range r_2 = [1.0, 2.5] Å) if present. CEP-4G bases and corresponding pseudopotentials[42] were employed for atoms in the outermost shell (typical shell range $r_3 \geq$ 2.5 Å) if present. For the heavier atoms Sr and Ba, the CEP-4G sets also substituted for the all-electron sets in the shell range r_2. The basis set for P atoms in the range r_3 was supplemented by a d function (Gaussian exponent = $0.55a^{-2}$).

The *Gaussian 03* program package[43] was used for electronic structure calculations within *EEIM* using the hybrid density functional mPW1PW[44] throughout with tight convergence criteria for the SCF and GIAO calculations. Quadrature in the DFT calculations was performed on a pruned grid of 99 radial shells and 590 angular points per shell on each atom. Atomic charges were obtained by NBO population analysis[45] and absolute nuclear magnetic shielding tensors $\tilde{\delta}$ by the GIAO method.[46]

The calculated absolute shielding tensors are usually nonsymmetric tensors. Because of the fact that experimentally obtainable chemical shift tensors contain only symmetric elements, the calculated shielding tensors were symmetrized. Subsequent diagonalization led to the principal axis values σ_{ii} and orientation of the PAS, given relative to (i) the molecular coordinate system that was used for the calculation. Furthermore, the PAS orientation was calculated relative to (ii) the orthogonalized crystal axis system (CRY) and (iii) a LCS defined by the position of the nucleus under investigation and its nearest neighbors. The relative orientations can be described in various ways, e.g., by Euler angles or by direction cosines.

For a comparison between the calculated principal axis values $\sigma_{ii,calc}$ of the absolute nuclear magnetic shielding tensors and the experimental principal axis values $\delta_{ii,exp}$ of the chemical shift tensors, a conversion equation is needed. In a first step, calculated shift values $\delta_{ii,calc}$ were obtained from the corresponding absolute shielding values $\sigma_{ii,calc}$ by the conversion equation

$$\delta_{ii,calc}^{^{31}P} = \frac{\delta_{ii,calc}^{^{31}P} - A}{B} \qquad i = 1 - 3 \tag{1}$$

with A = 303.29 ppm and B = −1.1174, that was derived in ref 20 for the mPW1PW/6-311G(3df,3dp) model.[47,48] Comparison of the calculated shifts obtained for the three P sites with the experimental NMR data allowed assignment of the experimentally observed NMR signals to crystallographic sites. Subsequently, a refined conversion equation with parameters A = 307.315 ppm and B = −1.04781 specific to the investigated aminotris(methylenephosphonates) was derived, which further improved the correlation between the calculated and experimental data.

RESULTS AND DISCUSSION

Crystal Structures of *M*AMP·xH_2O Salts. Crystal structures of *M*AMP with *M* = Zn, Mg, Ca, Sr, and (2Na) and x = 3, 3, 4.5, 0, and 1.5, respectively, were described in detail in previous papers.[24−27] In the following, we shortly want to discuss the changes obtained by the quantum-chemical structure optimizations and point out the similarities and differences between the various structures with a focus on the AMP^{2-} units that form different hydrogen-bonding networks. The refined H-atom positions from the structure optimizations in this work (see Tables S6–S12 in the SI) lead to longer covalent bond lengths and shorter hydrogen bridge bonds, in general, and thus a strengthened network. $ZnAMP{\cdot}3H_2O$ and $MgAMP{\cdot}3H_2O$ are members of the isostructural family $MAMP{\cdot}3H_2O$ that also includes the metal ions Co, Mn, Ni, and Cd,[49] in which the molecular structure of the AMP^{2-} unit is very similar. The same basic molecular conformation of AMP^{2-} is found in $CaAMP{\cdot}4.5H_2O$, SrAMP and BaAMP as well, despite the different coordination modes of the phosphonate groups in these compounds. Table 3 lists several structural data for the five above-mentioned *M*AMPs, which can be assumed to have a dominant effect on the ^{31}P chemical shift tensors of atoms Pi. Regarding the three distinct torsion angles $\lvert\tau$(Pi–C–N–H)$\rvert$ in an AMP^{2-} moiety (i = 1–3), two phosphonate groups possess a gauche confirmation and one a trans conformation relative to the H(N) proton, as shown for SrAMP in Figure 1 and for BaAMP in Figure 2. This is a

dx.doi.org/10.1021/ic301192y | Inorg. Chem. 2012, 51, 11466−11477

conspicuous characteristic feature of all five *M*AMP molecular structures.

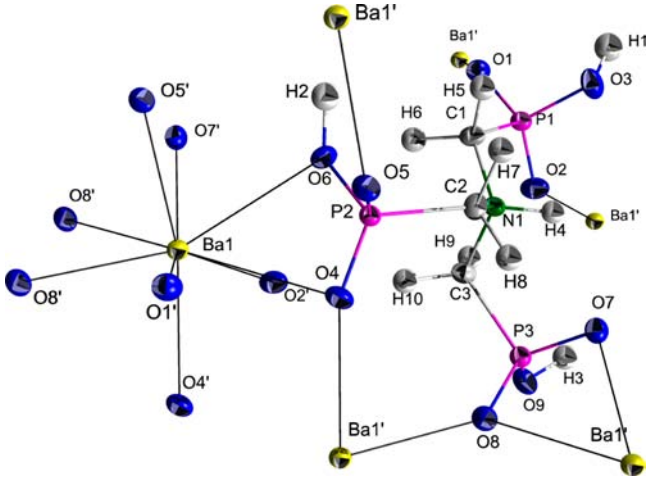

Figure 2. Coordination in BaAMP. The Ba atom is surrounded by nine O atoms. The AMP unit is coordinated by six Ba atoms via its O atoms. Site positions are indicated by 50% thermal ellipsoids, except for H atoms, which were not refined anisotropically.

It turns out, however, that these torsion angles |τ(P*i*−C−N−H)| are not helpful for the assignment of the P*i* crystal positions to the ^{31}P NMR signals (see the next section). The molecular structure of the AMP^{2-} unit in (2Na)AMP·1.5H_2O differs from the above-mentioned structures primarily by cis conformation of one phosphonate group beside two gauche groups.

Crystal Structure of Ba[HN(CH$_2$PO$_3$H)$_3$] (BaAMP). The basic conformation of the AMP^{2-} unit in this anhydrous polymorph is identical with those of the other *M*AMPs. The structure of BaAMP is a 2D-layered structure. The inorganic layer is composed of Ba^{2+} centers that are bridged by phosphonate O atoms to create a layer in the *ab* plane. One of the methylenephosphonate arms is extended to reach the neighboring inorganic layer, binding to two Ba atoms. This is shown in Figure S3 in the SI.

The coordination in BaAMP is shown in Figure 2. Each Ba center is nine-coordinated. The terminal O4 and O8 are connected with two Ba atoms and the other four terminal O atoms with only one Ba. It is worth noting that the protonated O6 also has contact with one Ba. Overall, phosphonate P2 has four O−Ba contacts to three Ba atoms, P3 has three O−Ba contacts to two Ba atoms and P1 two O−Ba contacts to two Ba atoms. The high coordination number of Ba leads to the formation of several rings including covalent bonds and to ionic connections with other BaAMP units. Two phosphonate fragments, O4−P2−O6 and O7−P3−O8, bind Ba in chelating fashions, forming two nonplanar four-membered rings. Another Ba atom is chelated by the fragment O4−P2−C2−N1−C3−P3−O8, thus forming an eight-membered ring.

Two fragments, O1−P1−O2 and O2′−P1′−O1′, form a centrosymmetric eight-membered ring with two Ba atoms. Planar four-membered rings are formed by two Ba with O4 and O4′ and also with O8 and O8′ (see Figure S4 in the SI). The Ba−O6(H) atomic distance is close to 3 Å, in the same range as the distances Ba−O4 and Ba−O8. This is at the "longer" limit of the Ba−O(P) bond distances commonly observed in barium phosphonates,[50] which are usually in the range 2.7−3.0 Å. The bond lengths and angles are given in Table 4 and the fractional coordinates for BaAMP in Table S5 in the SI.

Table 4. Selected Bond Lengths and Angles for BaAMP[a]

Bond Lengths (Å)			
Ba1−O4#1	2.6954	Ba1−O7	2.8851
Ba1−O2#1	2.7183	Ba1−O8	2.9464
Ba1−O8#2	2.7231	Ba1−O6	2.9933
Ba1−O5#3	2.7905	Ba1−O4	3.0401
Ba1−O1	2.8727		
C1−N1	1.5152	C3−N1	1.5123
C2−N1	1.5131		
Angles (deg)			
C1−P1−O1	105.6	O1−P1−O3	109.9
C1−P1−O2	109.5	O2−P1−O3	111.9
C1−P1−O3	101.5	O4−P2−O6	105.8
C2−P2−O4	111.0	O5−P2−O6	111.4
C2−P2−O5	103.2	O7−P3−O9	112.3
C2−P2−O6	107.7	O8−P3−O9	109.5
C3−P3−O7	105.0	C1−N1−C2	112.8
C3−P3−O8	112.8	C1−N1−C3	111.4
C3−P3−O9	103.1	C2−N1−C3	113.4
Torsion Angles (deg)			
P1−C1−N1−C2	156.6	P2−C2−N1−C1	73.0
P1−C1−N1−C3	−74.6	P2−C2−N1−C3	−54.7
P3−C3−N1−C1	153.0	P3−C3−N1−C2	−78.5

[a]Symmetry transformations used to generate equivalent atoms: #1, $-x+1, -y, -z+1$; #2, $-x+1, -y+1, -z+1$; #3, $-x, -y, -z+1$.

CP MAS ^{31}P NMR Spectra of *M*AMP·*x*H_2O Salts. The CP MAS $^{31}P\{^1H\}$ NMR sideband spectra of powdered samples of *M*AMP·*x*H_2O, where *M* = Zn, Mg, Ca, Sr, and Ba and *x* = 3, 3, 4.5, 0, and 0, respectively, are shown in Figure 3. Because the asymmetric unit in the crystal structures contains one molecule, we expect three sideband systems in the MAS ^{31}P NMR spectra for all *M*AMP compounds. The similarity of the spectra for the isostructural ZnAMP·3H_2O and MgAMP·3H_2O was expected. In contrast, the spectrum of CaAMP·4.5H_2O seems to possess only two isotropic chemical shifts at 11.7 and 4.4 ppm. However, the intensity ratio of the two signals is approximately 1:2, so that the NMR signal at 4.4 ppm must stem from two crystallographically nonequivalent P sites, which have nearly identical isotropic chemical shifts. This fact was noticed by Bishop et al.[13d] and explained by two bridging and one terminal phosphonate groups in CaAMP·4.5H_2O.

According to the nomenclature introduced by Massiot et al.[13b] regarding the description of connectivities, the bridging phosphonate groups P1 and P3 have the connectivity (110) to Ca ions (see Table 3), while the terminal phosphonate group P2 has (100). Similar bridging of two phosphonate groups alone is not sufficient to explain the similarity in the chemical shifts, however. For example, although SrAMP has two similar bridging phosphonate groups (P1 and P3), their δ_{iso} chemical shifts differ significantly.

Experimental ^{31}P chemical shifts δ_{iso} and shift tensor principal axis values δ_{ii} obtained from the CP/MAS spectra of all investigated *M*AMPs are summarized in Table 5. Note that the orientation of the shielding tensor PAS relative to a reference coordinate system remains open by MAS investigation of powders and that the assignment of the ^{31}P signals

dx.doi.org/10.1021/ic301192y | *Inorg. Chem.* 2012, 51, 11466−11477

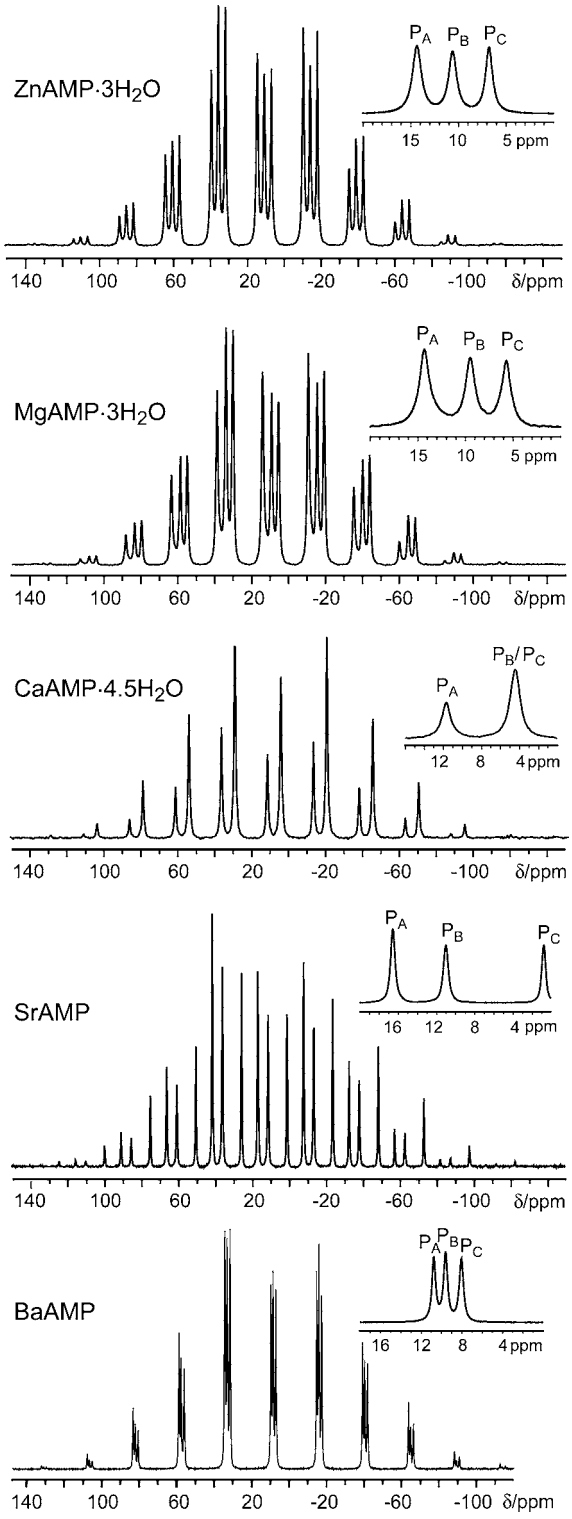

Figure 3. CP MAS ^{31}P NMR spectra of *M*AMP·xH$_2$O, where *M* = Zn, Mg, Ca, Sr, and Ba. Spectrometer frequency = 162.02 MHz, ν_{MAS} = 4 kHz, and t_{CP} = 5 ms. The isotropic chemical shifts δ_{iso} of different sideband systems are labeled as P_A, P_B, and P_C.

to the chemically very similar P sites in the crystal structure also stays open.

Empirical correlations between ^{31}P δ_{iso} or δ_{ii} values and structural parameters have been described in the literature for phosphates[51] and phosphonates.[13b] We made attempts to find empirical correlations for the assignment of δ_{iso} or δ_{ii} data of P_A, P_B, and P_C to structural parameters connected with the sites P1, P2, and P3. Our best attempt shows a satisfactory correlation (see Figure 4) between δ_{33} and the mean atomic distance of P*i* to the terminal O atoms, $\bar{d}(Pi{-}O_t) = [d(Pi{-}O_t) + d(Pi{-}O_{t'})]/2$, with a coefficient of determination $r^2 = 0.722$ and a standard deviation (SD) of the predicted value δ_{33} of ≈6 ppm. The origin of this correlation is discussed below together with the tensor orientations.

For SrAMP, the assignments $P_A \leftrightarrow$ P2, $P_B \leftrightarrow$ P1, and $P_C \leftrightarrow$ P3 and, for MgAMP·3H$_2$O, $P_A \leftrightarrow$ P1, $P_B \leftrightarrow$ P3, and $P_C \leftrightarrow$ P2 should be correct, but for the other *M*AMPs, the high SD does not allow a reliable assignment. This assignment problem of experimentally observed ^{31}P NMR signals to crystallographic sites was solved by our quantum-chemical calculations.

Calculations of ^{31}P Chemical Shift Tensors for *M*AMP·xH$_2$O Clusters. Calculations of ^{31}P chemical shift tensors $\vec{\vec{\delta}}$ for *M*AMP·xH$_2$O with *M* = Zn, Mg, Ca, Sr, and Ba were performed with the *EEIM* method at XRD structures with H-atom positions optimized by *VASP* (see Tables S6–S12 in the SI), as explained in the Computational Details section. The reliability of this approach is verified for $\vec{\vec{\delta}}^{31P}$ of (2-aminoethyl)-phosphonic acid in Chapter 9 of the SI, where calculated data agree well with experimental data from van Calsteren et al.[14a] showing deviations <2.8 ppm in the tensor eigenvalues and <2.7° in the eigenvector orientations only. At each *M*AMP structure, three different embedded QCs were chosen for checking the convergence of the embedding scheme, namely, the AMP^{2-} ion as well as the uncharged $[M\text{AMP}\cdot x\text{H}_2\text{O}]_1$ and $[M\text{AMP}\cdot x\text{H}_2\text{O}]_8$ clusters.

In the following, we focus the discussion on the most reliable results obtained with $[M\text{AMP}\cdot x\text{H}_2\text{O}]_8$ QCs, although most signal assignments can already be made on the basis calculations using AMP^{2-} as the QC. The calculated isotropic shifts δ_{iso} and shift tensor principal axis values δ_{ii} are listed in Table 5 together with experimental data.

The root-mean-square deviations rmsd(δ_{iso}^{exp},δ_{iso}^{calc}) = 0.89 ppm and rmsd(δ_{ii}^{exp},δ_{ii}^{calc}) = 3.4 ppm reflect an excellent agreement between both data sets, which is a necessary condition for an unambiguous assignment of the nearby NMR signals to crystallographic sites. A necessary requirement for the close agreement is, that the ^{31}P absolute nuclear magnetic shielding values σ_{ii} (see Table S15 in the SI) are converted to chemical shifts δ_{ii} by eq 1 using *M*AMP-specific parameters A = 307.315 ppm and B = −1.04781, which are obtained from the linear fit in Figure 5. The same signal assignment is also obtained when shifts δ_{iso}^{calc} and δ_{ii}^{calc} are calculated with the original A and B parameters from ref 20; however, these calculated shifts show a systematic deviation from the experimental ones.

We investigated the effect of four different input structures on the calculated ^{31}P shift tensors in the case of SrAMP, whose experimental NMR spectrum shows the biggest differences between the isotropic chemical shifts of P_A and P_B and also P_B and P_C. Calculations at the experimental XRD structure without refinement of the H-atom positions result in significantly increased rmsd(δ_{iso}^{exp},δ_{iso}^{calc}) and rmsd(δ_{ii}^{exp},δ_{ii}^{calc}) compared to the XRD structure with quantum chemically optimized H-atom positions (see Table S14 in the SI). Also, an optimization of all fractional coordinates or a full optimization including the unit cell vectors does not improve rmsd(δ_{ii}^{exp},δ_{ii}^{calc}). We conclude that the crystal structure from XRD with optimized H-atom positions is probably the most accurate one of the four and that the increased calculation times for

dx.doi.org/10.1021/ic301192y | *Inorg. Chem.* 2012, 51, 11466–11477

Table 5. Experimental and Calculated ^{31}P Chemical Shift Tensor Eigenvalues of Metal Aminotris(methylenephosphonates) (Calculated Values Obtained from *EEIM* Using $[MAMP{\cdot}xH_2O]_8$ Clusters)

			principal values of chemical shift tensors (ppm)							
	P site labels		δ_{iso}		δ_{11}		δ_{22}		δ_{33}	
*M*AMP·xH$_2$O	NMR	crystal position[a]	exp	calc	exp	calc	exp	calc	exp	calc
ZnAMP·3H$_2$O	P_A	P1	14.3(1)	14.4	88(2)	86.1	9(1)	7.9	−54(2)	−50.9
	P_B	P3	10.6(1)	11.1	87(3)	83.7	17(2)	16.7	−72(3)	−67.1
	P_C	P2	6.7(1)	4.4	85(5)	81.9	9(4)	5.4	−74(5)	−74.3
MgAMP·3H$_2$O	P_A	P1	14.3(1)	15.1	87(1)	87.1	10(1)	7.7	−54(1)	−49.5
	P_B	P3	9.5(1)	8.1	86(4)	84.5	17(6)	13.2	−75(4)	−73.4
	P_C	P2	5.7(1)	4.1	86(3)	83.8	11(2)	6.7	−80(3)	−78.3
(CaAMP)$_2$·9H$_2$O[b]	P_A	P2, P5	11.7(1)[c]	12.4	89(4)	86.8	14(5)	16.0	−68(4)	−65.6
	P_B	P3, P6	4.4(1)[c]	4.2	90(4)	93.7	6(4)	1.4	−83(4)	−82.5
	P_C	P1, P4	4.4(1)[c]	4.1	90(4)	85.6	6(4)	8.1	−83(4)	−81.4
SrAMP	P_A	P2	16.6(1)	17.2	88(2)	89.9	22(2)	21.4	−60(2)	−59.7
	P_B	P1	11.0(1)	11.6	83(2)	85.1	20(2)	20.5	−70(2)	−70.8
	P_C	P3	0.8(1)	2.8	93(4)	100.9	5(6)	2.1	−95(4)	−94.7
BaAMP	P_A	P1	10.8(1)	10.5	94(2)	97.6	17(1)	18.1	−79(2)	−84.1
	P_B	P2	9.6(1)	9.4	85(3)	89.1	11(2)	12.7	−67(3)	−73.5
	P_C	P3	8.1(1)	8.6	81(5)	90.1	16(5)	10.0	−73(5)	−74.3
(2Na)AMP·1.5H$_2$O[d]	P_A		14.0(1) [13.8]		95(3) [96]		12(2) [15]		−68(3) [−70]	
	P_B		12.9(1) [12.7]		97(4) [96]		9(2) [10]		−67(4) [−68]	
	P_C		11.7(1) [11.6]		99(4) [98]		2(2) [4]		−69(4) [−68]	

[a]For a better comparison of different *M*AMP crystal structures, the nonuniform labeling of atoms in previously published works was changed to a consistent labeling. Labels Pi (i = 1−3) for P atoms are chosen according to the following order of the torsion angles: $|\tau(P2{-}C{-}N{-}H)| > |\tau(P1{-}C{-}N{-}H)| > |\tau(P3{-}C{-}N{-}H)|$. The labels used in XRD and in this paper are juxtaposed in Tables S1−S5 in the SI. [b]The peculiarity of the $[(CaAMP)_2{\cdot}9H_2O]_4$ cluster calculation is described in the text. [c]In ref 13d, the same experimental isotropic chemical shifts of 11.7 and 4.4 ppm were found. [d]Values in square brackets are from ref 13e, in which (2Na)AMP·1.5H$_2$O was prepared by another method. The nearly identical chemical shift values indicate that the crystal structures of samples prepared according to refs 13e and 27 are the same.

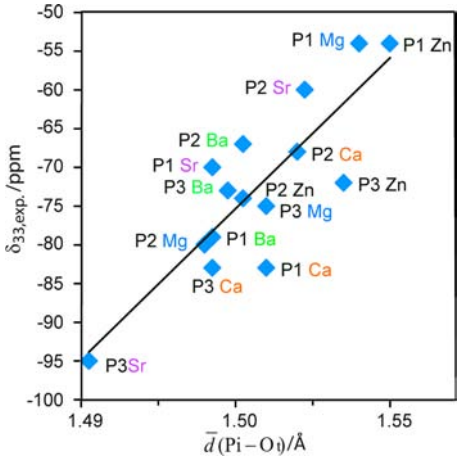

Figure 4. Correlation between the mean bond length $\bar{d}(Pi{-}O_t)$ and the principal values δ_{33} of the experimental ^{31}P chemical shift tensors in *M*AMP·xH$_2$O. The line results by a least-squares fit to the equation $\delta_{33} = A + B[\bar{d}(Pi{-}O_t)]$ with A = −3006.9 ppm, B = 1954.4 ppm/Å, and r^2 = 0.722.

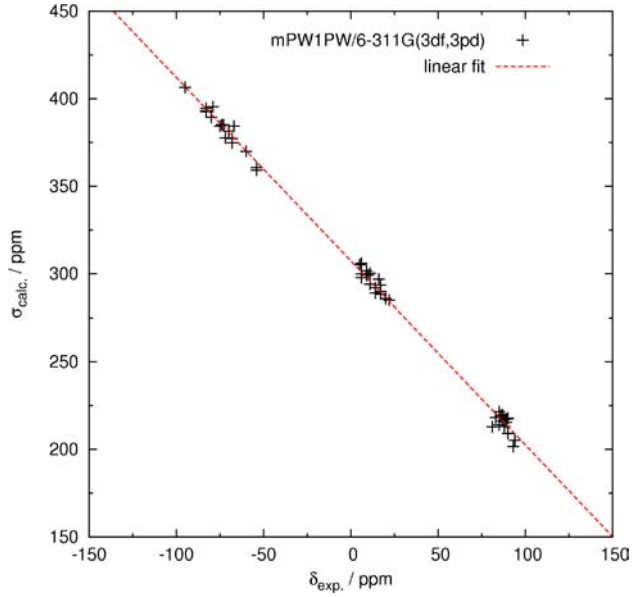

Figure 5. Correlation plot of 54 calculated principal axis values of ^{31}P magnetic shielding tensors in *M*AMP·xH$_2$O, with *M* = Zn Mg, Ca, Sr, and Ba, versus experimental principal axis values of the corresponding chemical shift tensors. The dashed red line shows the least-squares fit with A = 307.315 ppm, B = 1.04781, and r^2 = 0.998, leading to rmsd(δ_{ii}^{exp},δ_{ii}^{calc}) = 3.4 ppm.

extended PW91/PAW optimizations are at least unnecessary, if not counterproductive. This conclusion is in line with several previous works, which showed that periodic local-density approximation or GGA DFT optimizations on molecular crystals certainly improve the H-atom positions of experimental XRD structures but are inferior to high-quality XRD structures in other respects, especially the cell parameters.[52]

It is surprising that the calculations of simple clusters $[MAMP{\cdot}xH_2O]_1$ (except for $[BaAMP]_1$) and even of the ion AMP^{2-} already give the correct assignment, although rmsd-(δ^{exp},δ^{calc}) is significantly higher. This suggests that the main contributions to the ^{31}P shift tensors in *M*AMP·xH$_2$O are given by the induced currents within the AMP^{2-} unit.

dx.doi.org/10.1021/ic301192y | *Inorg. Chem.* 2012, 51, 11466−11477

The construction of embedded clusters for CaAMP·4.5H_2O is complicated by the presence of partially occupied atomic sites of one H_2O molecule in the reported crystal structure. The question arises about which manner this H_2O is present in the crystal. Either a static or dynamic disorder or an ordered superstructure in different crystal domains might be present.

Thus, we defined a superstructure $(CaAMP)_2·9H_2O$, where the formerly half-occupied sites are changed to an alternating pattern of fully occupied and empty sites. Decreasing in this way the symmetry of the crystal structure from $P2_1/n$ to $P2_1$[53] (see Figures S13−S15 in the SI), the asymmetric unit contains two different AMP molecules and the calculation gives six phosphorus tensors: P1, P2, and P3 for one AMP unit and P4, P5, and P6 for the other. The calculated isotropic chemical shifts are 4.36, 12.98, and 3.91 ppm for the first AMP unit and 3.84, 11.82, and 4.54 ppm for the second. If such an ordered superstructure would really exist, we would expect the experimentally observed signal P_A at 11.7 ppm to be split into two distinct lines with a distance of more than 1 ppm (see Figure S11 in the SI). A static disorder is equally unlikely because we would expect a significantly broader signal for P_A than the observed one, whose line width of 180 Hz is comparable to the signal widths of the other H_2O-containing *M*AMPs. Hence, a dynamic disorder, i.e., a fast exchange of the H_2O molecule between the "occupied" and "empty" sites of the ordered superstructure, must be present. Fast exchange is possible because each "occupied" site has a vicinal "empty" site at a distance of 1.53 Å for the O atom and of 0.49 Å for the H atoms only (see Figure S14 in the SI). If the dynamics are fast on the time scales of XRD and NMR, this explains the split sites with large thermal ellipsoids (50% probability ellipsoids of partially occupied "O1S" sites in ref 13d are overlapping) in the first case, as well as the single line for P_A caused by motional averaging in the NMR spectrum. Attempts to freeze the dynamics were unsuccessful. Fast motion is maintained at temperatures down to 170 K, where low-temperature CP MAS ^{31}P NMR spectra show only a slight signal broadening and a small signal shift (see Figure S16 in the SI) and the XRD pattern shows no indication for a superstructure. XRD measurements at temperatures down to 10 K required evacuation of the irradiation chamber, upon which the structure of CaAMP·4.5H_2O decomposed under loss of crystal water into a partly amorphous solid with a largely altered XRD pattern. The H_2O loss is (at least partly) reversible because the old reflections reoccurred when the sample was exposed to humid air for 5 days (see Figure S17 in the SI).

Reducing the six calculated shift values of the superstructure to three mean values of corresponding pairs (P1, P4; P2, P5; and P3, P6), we simulate a fast exchange and reconstruct the high symmetry of CaAMP·4.5H_2O obtained by X-ray structure. The chemical shift data calculated in this way are in good agreement with experimental data not only with respect to the isotropic shifts (calculated values of P_B and P_C differ by 0.1 ppm, only, which explains why the signals could not be resolved experimentally) but also with respect to the intensity pattern of the rotational sidebands for signal group $P_{B/C}$, which is a superposition of the two (averaged) sideband systems (P1, P4) and (P3, P6), whose corresponding principal axis values δ_{11} and δ_{22} differ by 7−8 ppm in opposite directions. As shown in Figure S12 in the SI, the superposition of the calculated signals results in excellent agreement with the experimental intensity pattern for $P_{B/C}$, whereas the individually simulated spectra of (P1, P4) and (P3, P6) alone could not explain the near mirror symmetry of the experimental sideband pattern.

Tensor Orientation of Monoprotonated Phosphonates. For convenience, we look at the ^{31}P *absolute magnetic shielding tensors* $\vec{\sigma}$ rather than the chemical shift tensors $\vec{\delta}$ in this section; $\vec{\sigma}$ is directly related to the electronic environment of a nucleus, while $\vec{\delta}$ is a quantity that is defined relative to a reference compound. The directions of $\vec{\sigma}$ principal axes are the same as those of $\vec{\delta}$. They were obtained along with the principal axis values σ_{ii} by quantum-chemical calculations as direction cosines relative to the used coordinate system. Each of the three crystallographically different P atoms in the AMP unit possesses its own principal axis orientation. As an example, Figure 6 shows the symmetric shielding tensors of the AMP unit in SrAMP in the so-called "ovaloid representation".[54,55] In this figure, the directions of the principal axes are drawn as unit vectors ($\mathbf{e}_1^{PAS}$, $\mathbf{e}_2^{PAS}$, $\mathbf{e}_3^{PAS}$), where it is implicitly clear that each individual vector could point in its opposite direction just as well.[56] For a better comparison (see below), we always choose a right-handed PAS and select $\mathbf{e}_1^{PAS}$ and $\mathbf{e}_2^{PAS}$ to have an acute angle with the P−C bond and O═P═O angle bisector, respectively.

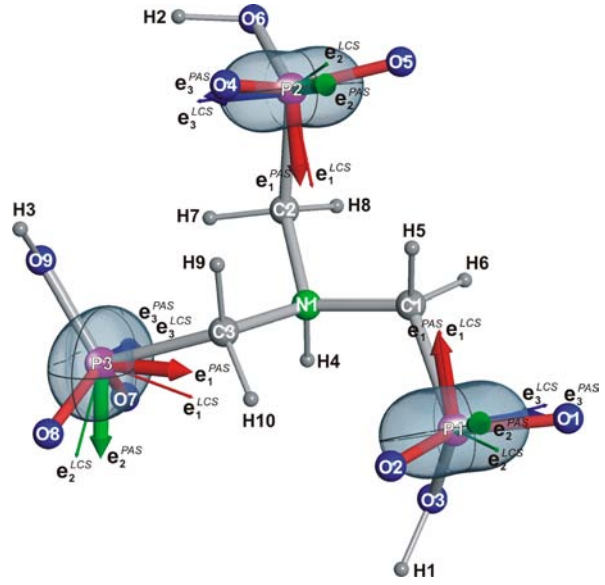

Figure 6. Ovaloid representation of the ^{31}P nuclear magnetic shielding tensors for SrAMP calculated by the *EEIM* method. At each P atom, thick arrows in red, green, and blue denote the principal axis vectors $\mathbf{e}_1^{PAS}$, $\mathbf{e}_2^{PAS}$, and $\mathbf{e}_3^{PAS}$, respectively. Thin arrows indicate the basis vectors of the LCS; see the text for details. The relative distances from a P atom to the vertices of the ovaloid are proportional to the relative sizes of the principal axis values σ_{ii}. The P−$O_{t/t'}$ bonds, which play a prominent role for magnitude and orientation of the shielding tensor, are highlighted in red.

It is obvious that the PAS orientations for the three P atoms, although very different in a general coordinate system, are similarly oriented with respect to their local environment: (i) the basis vector $\mathbf{e}_1^{PAS}$ lies roughly in the direction of the cross product of the two vectors from P to the terminal atoms O_t and $O_{t'}$, (ii) $\mathbf{e}_2^{PAS}$ bisects approximately the angle between the two terminal P−$O_{t/t'}$ bonds, and (iii) $\mathbf{e}_3^{PAS}$ points nearly in the direction of the cross product of the two directions defined in i and ii or, similarly, in the direction of the normal vector of the plane spanned by C−P−O(H). This direction may be regarded

dx.doi.org/10.1021/ic301192y | *Inorg. Chem.* 2012, 51, 11466−11477

as a mirror plane of the local C_s pseudosymmetry of each phosphonate group $-CPO_2O(H)$.

For a comparison of the tensor orientations of different phosphonate groups in the same and in other *M*AMPs, it is suitable to choose an LCS that reflects the C_s pseudosymmetry of the phosphonate group. LCSs were used previously as reference axis systems, in which the tensor PAS could be described by means of direction cosines, e.g., in refs 14a and 16a. The proposed definition of an LCS by Van Calsteren et al.[14a] for phosphonates is ambiguous, however. A non-ambiguous LCS can be defined as follows:

(i) The position vectors of the P atom, its C-atom neighbor, and its nearest and second-nearest O atoms are labeled as **P**, **C**, $\mathbf{O}_t$, and $\mathbf{O}_{t'}$, respectively. We may define three auxiliary vectors $\mathbf{e}_C$, $\mathbf{e}_t$, and $\mathbf{e}_{t'}$ as

$$\mathbf{e}_C = \frac{\mathbf{C} - \mathbf{P}}{|\mathbf{C} - \mathbf{P}|}; \quad \mathbf{e}_t = \frac{\mathbf{O}_t - \mathbf{P}}{|\mathbf{O}_t - \mathbf{P}|}; \quad \mathbf{e}_{t'} = \frac{\mathbf{O}_{t'} - \mathbf{P}}{|\mathbf{O}_{t'} - \mathbf{P}|} \tag{2}$$

which help to establish the basis vectors of the LCS.

(ii) The basis vectors of the LCS are then defined by

$$\mathbf{e}_1^{LCS} = \pm\frac{\mathbf{e}_t \times \mathbf{e}_{t'}}{|\mathbf{e}_t \times \mathbf{e}_{t'}|} \tag{3}$$

$$\mathbf{e}_2^{LCS} = \frac{\mathbf{e}_t + \mathbf{e}_{t'}}{|\mathbf{e}_t + \mathbf{e}_{t'}|} \tag{4}$$

$$\mathbf{e}_3^{LCS} = \mathbf{e}_1^{LCS} \times \mathbf{e}_2^{LCS} \tag{5}$$

The sign in eq 3 is chosen in such a way that the angle between $\mathbf{e}_1^{LCS}$ and $\mathbf{e}_C$ is acute (<90°).

The definition is convenient because it relates the LCS essentially with a pseudo-C_{2v}-symmetric $O_t-P-O_{t'}$ fragment (the two shortest P−O bonds are of approximately equal length), which is expected to contribute the most significant part to the ^{31}P magnetic shielding because there are more electrons at a closer distance to P in that fragment than in any other pair of nearest neighbors plus the P atom itself. Consequently, we expect small ^{31}P shielding along the direction $\mathbf{e}_1^{LCS}$, which is perpendicular to the plane spanned by $O_t-P-O_{t'}$, larger shielding along $\mathbf{e}_2^{LCS}$, and the largest shielding approximately along $\mathbf{e}_3^{LCS}$, which has the smallest angles with the short P−O bonds.[57] This is affirmed by the rather small angular deviations, $\alpha_{ii} = \text{acos}(\mathbf{e}_i^{PAS}\cdot\mathbf{e}_i^{LCS})$ with i = 1−3, between $\mathbf{e}_i^{PAS}$ and $\mathbf{e}_1^{LCS}$, $\mathbf{e}_2^{PAS}$ and $\mathbf{e}_2^{LCS}$, and $\mathbf{e}_3^{PAS}$ and $\mathbf{e}_3^{LCS}$, which are shown in Table 6. Although not a complete specification of the PAS orientation, these angles give a good impression of the PAS deviation relative to the LCS. Full PAS orientations relative to the LCS or CRY in terms of direction cosines or Euler angles are omitted for brevity here but are given in the Supporting Information (Tables S16−S25).

The angular deviations between the directions of $\mathbf{e}_1^{PAS}$ and $\mathbf{e}_1^{LCS}$ for the calculated compounds amount to 12−19° (or expressed as a range around the mean value α_{11} = 15.7° ± 3.9°), of $\mathbf{e}_2^{PAS}$ and $\mathbf{e}_2^{LCS}$ to 12−24° (mean value α_{22} = 16.6° ± 7.7°), and of $\mathbf{e}_3^{PAS}$ and $\mathbf{e}_3^{LCS}$ to 1−18° (mean value α_{33} = 6.7° ± 11.4°). The small angular deviation between $\mathbf{e}_3^{PAS}$ and $\mathbf{e}_3^{LCS}$ can be explained by the fact that both axes are virtually perpendicular to the σ_h mirror plane of the pseudosymmetry C_s. BaAMP is special in this respect: its α_{33} values of 12.3° (P1) and 18.1° (P3) are significantly larger than those obtained for P atoms of the other compounds. This correlates with significantly larger bond length differences $|d(PO_{t'}) - d(PO_t)|$ in BaAMP (see Table 3), which show values up to 0.028 Å and thus reflect larger deviations from the idealized C_s symmetry of $-CPO_2O(H)$. Excluding BaAMP, the mean value and range would be α_{33} = 5.4° ± 4.4°. The rather narrow ranges around the arithmetic mean in all α_{ii} and the fact that the direction of the angular deviations is systematic (see Table 7) indicate that phosphonate groups possess a characteristic ^{31}P shielding tensor orientation relative to the LCS or ultimately the atomic coordinates of the $-CPO_2O(H)$ unit. This knowledge may be used to derive structural information from experimentally determined shielding tensors, which is especially desirable for disordered or complex systems whose structure is not amenable via XRD techniques.

Table 6. Angular Deviations α_{ii} = acos($\mathbf{e}_i^{PAS}\cdot\mathbf{e}_i^{LCS}$) for ^{31}P Shielding Tensors Calculated by the *EEIM* Method for *M*AMP·xH$_2$O Compounds

QC	site	α_{11}/deg	α_{22}/deg	α_{33}/deg
$[ZnAMP\cdot3H_2O]_8$	P1	16.2	17.8	8.6
	P2	14.8	14.7	5.2
	P3	17.6	17.2	4.6
$[MgAMP\cdot3H_2O]_8$	P1	16.7	17.5	7.2
	P2	15.5	16.0	6.5
	P3	17.8	17.3	4.2
$[(CaAMP)_2\cdot9H_2O]_4$	P1	19.0	20.4	8.1
	P2	11.8	11.9	6.1
	P3	11.9	11.9	2.9
	P4	19.2	20.7	8.4
	P5	15.4	15.0	5.6
	P6	11.8	11.6	2.2
tensor averaging in LCS basis: $[Pi + P(i+3)]/2$	(P1, P4)	19.1	20.6	8.3
	(P2, P5)	13.6	13.4	5.8
	(P3, P6)	11.8	11.7	2.4
$[SrAMP]_8$	P1	17.7	17.0	6.0
	P2	11.8	12.5	5.0
	P3	14.7	14.8	1.1
$[BaAMP]_8$	P1	18.1	20.2	12.2
	P2	15.6	17.6	9.1
	P3	16.4	24.2	18.1

Table 7 shows the generic shielding tensor orientation of (aminomethylene)phosphonates obtained by averaging over n = 18 *M*AMP shielding tensor orientations $\Omega(n) = \{\mathbf{e}_1^{PAS}(n), \mathbf{e}_2^{PAS}(n)$, and $\mathbf{e}_3^{PAS}(n)\}$ expressed in LCSs in Tables S16−S20 in the SI.

The averaging is performed as follows: Three auxiliary vectors $\mathbf{r}_i$ (i = 1−3) are defined by

$$\mathbf{r}_i = \sum_n \mathbf{e}_i^{\text{PAS in LCS}}(n)/|\{\sum_n \mathbf{e}_i^{\text{PAS in LCS}}(n)\}| \tag{6}$$

The three $\mathbf{r}_i$ are normalized but not strictly orthogonal to each other. Subsequently, averaged orthonormal eigenvectors $\mathbf{e}_i^{av,PAS}$ denoted in the LCS are obtained by Gram-Schmidt orthogonalization of $\{\mathbf{r}_1, \mathbf{r}_2, \mathbf{r}_3\}$, where $\mathbf{r}_1$ is used as the starting vector.

Figure 7 shows the averaged absolute ^{31}P magnetic shielding tensor of all investigated $-CPO_2O(H)$ units in the ovaloid representation. The averaged tensor orientation from Table 7 was used together with principal axis values σ_{11} = 214.6 ppm, σ_{22} = 296.0 ppm, and σ_{33} = 383.6 ppm, obtained from averaging over the individual P sites listed in Table S15 in the SI. The shape of the ovaloid is characteristic for the phosphonate

dx.doi.org/10.1021/ic301192y | Inorg. Chem. 2012, 51, 11466−11477

Table 7. Average ^{31}P Magnetic Shielding Tensor Orientation of Phosphonates, Derived from the Tensor Orientations in *M*AMP·*x*H_2O Calculated in This Work[a]

eigenvector	$\mathbf{e}_1^{LCS}$	$\mathbf{e}_2^{LCS}$	$\mathbf{e}_3^{LCS}$	euler angles PAS → LCS		euler angles LCS → PAS		angular deviation α_{ii}	
$\mathbf{e}_1^{av,PAS}$	0.971364	−0.236551	0.022272	α_{PL}	314.56	α_{LP}	120.86	α_{11}	13.74
$\mathbf{e}_2^{av,PAS}$	0.237039	0.971237	−0.022614	β_{PL}	1.82	β_{LP}	1.82	α_{22}	13.78
$\mathbf{e}_3^{av,PAS}$	−0.016282	0.027246	0.999496	γ_{PL}	59.14	γ_{LP}	225.44	α_{33}	1.82

[a]Normalized principal axis vectors $\mathbf{e}_i^{av,PAS}$ are given in terms of direction cosines to the basis vectors of the LCS, defined in the text. Euler angles are given for Euler rotation according to Rose convention [58] from the PAS to the LCS and vice versa. The last column gives the angular deviation α_{ii} = acos($\mathbf{e}_i^{av,PAS}$·$\mathbf{e}_i^{LCS}$) between $\mathbf{e}_i^{av,PAS}$ and $\mathbf{e}_i^{LCS}$. All angles are expressed in degrees.

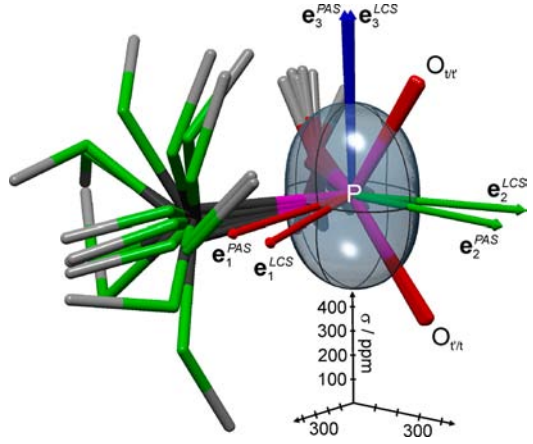

Figure 7. Ovaloid representation of the averaged absolute ^{31}P nuclear magnetic shielding tensor in monoprotonated (aminomethyl)-phosphonates (gray surface). Additionally, an overlay of stick models of the contributing molecular fragments H−N−C−PO_2−O(H) is shown where H atoms on C atoms were omitted for clarity. The basis vectors of the PAS and LCS have been stretched by a factor of 2.

compound class, and the small variations of shielding tensors of individual compounds are hardly visible in such representations.

CONCLUSIONS

In this contribution, we derived the average orientation of the ^{31}P NMR shielding tensor of monoprotonated phosphonates (−CPO_2OH) from five crystalline compounds with 18 different shielding tensors. In a suitably chosen LCS defined by the P−O and P−C bonds, all ^{31}P shielding tensors show a major resemblance and reflect the local C_s pseudosymmetry of the phosphonate group (−CPO_2O−) as well as the deviation from C_{2v} pseudosymmetry dictated by the O_t−P−$O_{t'}$ fragment (see Figure 7). The ^{31}P NMR tensor principal axes are close to the LCS axes, where a larger fraction of the deviation is systematic and could be incorporated into a refined empirical correlation between the local structure and orientation. In view of the reported statistical deviations, we anticipate a usage of the tensor orientations of phosphonate groups in phosphonolipids in a way similar to that shown in refs 17 for phosphate groups in phospholipids whose orientation in membranes could be investigated by ^{31}P NMR.

Furthermore, quantum-chemical *EEIM* calculations permitted an assignment of experimentally observed signals in MAS ^{31}P NMR powder spectra of *M*AMP·*x*H_2O (*M* = Zn, Mg, Ca, Sr, and Ba and *x* = 3, 3, 4.5, 0, and 0) to the crystallographic P sites (see Table 5). Accurate crystal structures are a necessary prerequisite for the reliable calculation of NMR parameters. Analysis of the rmsd's between experimental and calculated data of rmsd(δ_{ii}^{exp},δ_{ii}^{calc}) = 3.4 ppm for the principal axis values and rmsd(δ_{iso}^{exp},δ_{iso}^{calc}) = 0.89 ppm for the isotropic chemical shifts indicates that it is necessary and sufficient to refine the H-atom positions of XRD structures by partial, quantum-chemical structure optimizations under periodic boundary conditions (*VASP* program, PW91/PAW level) to obtain reliable predictions of the shielding parameters.

Dynamical disorder was found for the crystal structure of CaAMP·4.5H_2O. ^{31}P NMR parameters calculated for an ordered, static superstructure, $(CaAMP)_2$·9H_2O, ruled out the possibility of a static disorder. Experimentally observed ^{31}P NMR signal line shapes could be reproduced by averaging of inequivalent (though very similar) shielding tensors of the superstructure. This procedure should be applicable to calculate NMR parameters of disordered structures with fast dynamics in general.

ASSOCIATED CONTENT

Supporting Information

Listings of 19 figures and 27 tables as well as separate CIF files, XYZ files, and self-consistent point charge files for the embedded clusters. This material is available free of charge via the Internet at http://pubs.acs.org.

AUTHOR INFORMATION

Corresponding Author

*E-mail: demadis@chemistry.uoc.gr (K.D.D.), gunnej@cup.uni-muenchen.de (J.S.a.d.G.).

Notes

The authors declare no competing financial interest.

ACKNOWLEDGMENTS

K.D.D. thanks the General Secretariat of Science & Technology for partial funding (Project 2006-207c). J.S.a.d.G. and J.W. thank the Leibniz-Rechenzentrum for computational resources. This work was funded by the Deutsche Forschungsgemeinschaft (Emmy-Noether Program SCHM1570-2/1).

REFERENCES

(1) (a) Vioux, A.; Le Bideau, J.; Mutin, P. H.; Leclercq, D. *Top. Curr. Chem.* **2004**, *232*, 145−174. (b) Maeda, K. *Microporous Mesoporous Mater.* **2004**, *73*, 47−55. (c) Miller, S. R.; Pearce, G. M.; Wright, P. A.; Bonino, F.; Chavan, S.; Bordiga, S.; Margiolaki, I.; Guillou, N.; Férey, G.; Bourrelly, S.; Llewellyn, P. L. *J. Am. Chem. Soc.* **2008**, *130*, 15967−15981. (d) Liang, J.; Shimizu, G. K. H. *Inorg. Chem.* **2007**, *46*, 10449−10451.

(2) (a) Surblé, S.; Millange, F.; Serre, C.; Düren, T.; Latroche, M.; Bourrelly, S.; Llewellyn, P. L.; Férey, G. *J. Am. Chem. Soc.* **2006**, *128*, 14889−14896. (b) Horike, S.; Shimomura, S.; Kitagawa, S.. *Nat. Chem.* **2009**, *1*, 695−704.

(3) (a) Plabst, M.; McCusker, L. B.; Bein, T. *J. Am. Chem. Soc.* **2009**, *131*, 18112−18118. (b) Clearfield, A. *Solvent Extr. Ion Exch.* **2000**, *18*, 655−678. (c) Bortun, A. I.; Bortun, L. N.; Clearfield, A.; Khainakov, S. A.; García, J. *Solvent Extr. Ion Exch.* **1998**, *16*, 651−667. (d) Dalrymple, S. A.; Shimizu, G. K. H. *Chem.—Eur. J.* **2002**, *8*, 3010−3015.

(4) (a) Sava, D. F.; Kravtsov, V. C.; Nouar, F.; Wojtas, L.; Eubank, J. F.; Eddaoudi, M. *J. Am. Chem. Soc.* **2008**, *130*, 3768−3770. (b) Nouar, F.; Eckert, J.; Eubank, J. F.; Forster, P.; Eddaoudi, M. *J. Am. Chem. Soc.* **2009**, *131*, 2864−2870.
(5) (a) Zieba, A.; Sethuraman, G.; Perez, F.; Nancollas, G. H.; Cameron, D. *Langmuir* **1996**, *12*, 2853−2858. (b) Amjad, Z. *Langmuir* **1991**, *7*, 600−603. (c) Black, S. N.; Bromley, L. A.; Cottier, D.; Davey, R. J.; Dobbs, B.; Rout, J. E. *J. Chem. Soc., Faraday Trans.* **1991**, *87*, 3409−3414. (d) Pompe, E.; Lehman, H.-A. *Z. Anorg. Allg. Chem.* **1983**, *505*, 201−208. (e) Sweeney, F. M.; Cooper, S. D. *Society of Petroleum Engineers International Symposium on Oilfield Chemistry*, New Orleans, LA, March 2−5, 1993; paper SPE 25159.
(6) (a) Oddo, J. E.; Tomson, M. B. National Association of Corrosion Engineers, Houston, TX, 1992; Corrosion/92, Paper 34. (b) Xiao, J.; Kan, A. T.; Tomson, M. B. *Prepr. Symp.—Am. Chem. Soc., Div. Fuel Chem.* **1998**, *43*, 246. (c) Oddo, J. E.; Tomson, M. B. SPE Production & Facilities, Feb 1994; p 47.
(7) (a) Kesanli, B.; Lin, W. *Coord. Chem. Rev.* **2003**, *246*, 305−326. (b) Hu, A.; Ngo, H. L.; Lin, W. *J. Am. Chem. Soc.* **2003**, *125*, 11490−11491. (c) Forster, P. M.; Cheetham, A. K. *Top. Catal.* **2003**, *24*, 79−86.
(8) (a) Golomb, G.; Schlossman, A.; Saadeh, H.; Levi, M.; van Gelder, J. M.; Breuer, E. *Pharm. Res.* **1992**, *9*, 143−148. (b) Golomb, G.; Schlossman, A.; Eitan, Y.; Saadeh, H.; van Gelder, J. M.; Breuer, E. *J. Pharm. Sci.* **1992**, *81*, 1004−1007. (c) Sparidans, R. W.; Twiss, I. M.; Talbot, S. *Pharm. World Sci.* **1998**, *20*, 206−213. (d) Fleisch, H. *Drugs* **1991**, *42*, 919−944. (e) Hilderbrand, R. L., Ed. *The Role of Phosphonates in Living Systems*; CRC Press: Boca Raton, FL, 1983. (f) Fleisch, H. *Bone* **1987**, *8*, S23−S28. (g) Rubin, R. P.; Weiss, G. B.; Putney, J. W., Jr. *Calcium in Biological Systems*; Plenum Press: New York, 1985. (h) Fleisch, H. *Bisphosphonates in Bone Disease. From the Laboratory to the Patient*, 2nd ed.; The Parthenon Publishing Group: New York, 1995.
(9) (a) Ternan, N. G.; McGrath, J. W.; McMullan, G; Quinn, J. P. *World J. Microbiol. Biotechnol.* **1998**, *14*, 635−647. (b) Myong, N. U.S. Patent 4,268,507, 1981. (c) Gosselin, G.; Imbach, J.-L. FR Patent 2691463, 1993. (d) Hadden, J. W.; Giner-Sorolla, A. U.S. Patent 5,614,504, 1997. (e) Chintalapati, M.; Truax, R.; Stout, R.; Portier, R.; Losso, J. N. *J. Agric. Food Chem.* **2009**, *57*, 5201−5210.
(10) Dill, G. M.; Sammons, R. D.; Feng, P. C. C.; Kohn, F.; Kretzmer, K.; Mehrsheikh, A.; Bleeke, M.; Honegger, J. L.; Farmer, D.; Wright, D.; Haupfear, E. A. In *Glyphosate Resistance in Crops and Weeds: History, Development, and Management*; Nandula, V. K., Ed.; John Wiley & Sons: New York, 2010; pp 1−33.
(11) Mukhamedova, Kh. S.; Glushenkova, A. I. *Chem. Nat. Compd.* **2000**, *36*, 329−341.
(12) Tan, S. A.; Tan, L. G. *Clin. Physiol. Biochem.* **1989**, *7*, 303−309.
(13) (a) Harris, R. K.; Merwin, L. H.; Hägele, G. *Magn. Reson. Chem.* **1989**, *27*, 470−475. (b) Massiot, D.; Drummel, S.; Janvier, P.; Bujoli-Doeuff, M.; Bujoli, B. *Chem. Mater.* **1997**, *9*, 6−7. (c) Grossmann, G.; Grossmann, A.; Ohms, G.; Breuer, E.; Chen, R.; Golomb, G.; Cohen, H.; Hägele, G.; Classen, R. *Magn. Reson. Chem.* **2000**, *38*, 11−16. (d) Bishop, M.; Bott, S. G.; Barron, A. R. *Chem. Mater.* **2003**, *15*, 3074−3088. (e) Grossmann, G.; Burkov, K. A.; Hägele, G.; Myund, L. A.; Verwey, C.; Hermens, S.; Arat-ool, S. M. *Inorg. Chim. Acta* **2004**, *357*, 797−808. (f) Bakhmutova-Albert, E. V.; Bestaoui, N.; Bakhmutov, V. I.; Clearfield, A.; Rodriguez, A. V.; Llavona, R. *Inorg. Chem.* **2004**, *43*, 1264−1272. (g) Jankowski, S.; Huben, K.; Paneth, P.; Ciesielski, W.; Quin, L. D.; Vokal, B.; Dolenec, T. *Pol. J. Chem.* **2005**, *79*, 573−581. (h) Demadis, K. D.; Stavgianoudaki, N.; Grossmann, G.; Gruner, M.; Schwartz, J. L. *Inorg. Chem.* **2009**, *48*, 4154−4164. (i) Gehman, J. D.; Luc, F.; Hall, K.; Lee, T.-H.; Boland, M. P.; Pukala, T. L.; Bowie, J. H.; Aguilar, M.-I.; Separovic, F. *Biochemistry* **2008**, *47*, 8557−8565. (j) Klose, G.; Trahms, L.; Möps, A. *Chem. Phys. Lett.* **1985**, *122*, 545−549. (k) Jarrel, H. C.; Byrd, R. A.; Deslauriers, R.; Ekiel, I.; Smith, I. C. P. *Biochim. Biophys. Acta* **1981**, *648*, 80−86.
(14) (a) Van Calsteren, M.-R.; Birnbaum, G. I.; Smith, C. P. *J. Chem. Phys.* **1987**, *86*, 5405−5410. (b) Zhang, Y.; Oldfield, E. *J. Phys. Chem. B* **2004**, *108*, 19533−19540. (c) Rohonczy, J.; Ermark, F.; Haeberlen, U.; Klose, G.; Schulz, M. *Chem. Phys. Lett.* **1991**, *180*, 23−27.
(15) (a) Grossmann, G.; Krüger, K.; Ohms, G.; Fischer, A.; Jones, P. G.; Goerlich, J.; Schmutzler, R. *Inorg. Chem.* **1997**, *36*, 770−775. (b) Hahn, J.; Drexler, U.; Oimann, S.; Grossmann, G.; Ohms, G.; Krüger, K. *Phosphorus, Sulfur, Silicon* **1996**, *116*, 133−152.
(16) (a) Kohler, S. J.; Klein, M. P. *J. Am. Chem. Soc.* **1977**, *99*, 8290−8293. (b) Tutunjian, P.; Tropp, J.; Waugh, J. *J. Am. Chem. Soc.* **1983**, *105*, 4848−4849.
(17) (a) Griffin, R. G.; Powers, L.; Pershan, P. S. *Biochemistry* **1978**, *17*, 2718−2722. (b) Herzfeld, J.; Griffin, R. G.; Haberkorn, R. A. *Biochemistry* **1978**, *17*, 2711−2718. (c) Kohler, S. J.; Klein, M. P. *Biochemistry* **1976**, *15*, 967−973. (d) Kohler, S. J.; Klein, M. P. *Biochemistry* **1977**, *16*, 519−526. (e) Murray, D. K.; Harrison, J. C.; Wallace, W. E. *J. Colloid Interface Sci.* **2005**, *288*, 166−170.
(18) Lauterbur, P. C. *Phys. Rev. Lett.* **1958**, *1*, 343−344.
(19) (a) Weller, T.; Franck, U.; Klose, G.; Lochmann, R. *Z. Chem.* **1982**, *22*, 62. (b) Weller, T.; Franck, U.; Klose, G.; Lochmann, R. *Stud. Biophys.* **1983**, *93*, 275.
(20) Weber, J.; Schmedt auf der Günne, J. *Phys. Chem. Chem. Phys.* **2010**, *12*, 583−603.
(21) (a) Demadis, K. D.; Mavredaki, E. *Environ. Chem. Lett.* **2005**, *3*, 127−131. (b) El-Shall, H.; Rashad, M. M.; Abdel-Aal, E. A. *Cryst. Res. Technol.* **2002**, *37*, 1264−1273. (c) Pradip, R. B.; Rao, T. K.; Krishnamurthy, S.; Vetrivel, R.; Mielczarski, J.; Cases, J. M. *Langmuir* **2002**, *18*, 932−940. (d) Demadis, K. D.; Yang, B.; Young, P. R.; Kouznetsov, D. L.; Kelley, D. G. In *Advances in Crystal Growth Inhibition Technologies*; Amjad, Z., Ed.; Plenum Publishing Corp.: New York: 2000; Chapter 16, p 215.
(22) (a) Moedritzer, K.; Irani, R. R. *J. Org. Chem.* **1966**, *31*, 1603−1607. (b) Mund, L. A.; Arat-ool, Sh. M.; Busko, E. A.; Burkov, K. A. *Zh. Prikl. Khim.* **1995**, *68*, 736−740.
(23) Daly, J. J.; Wheatley, P. J. *J. Chem. Soc. A* **1967**, 212−221.
(24) Demadis, K. D.; Katarachia, S. D.; Koutmos, M. *Inorg. Chem. Commun.* **2005**, *8*, 254−258.
(25) Demadis, K. D.; Katarachia, S. D.; Raptis, R. G.; Zhao, H.; Baran, P. *Cryst. Growth Des.* **2006**, *6*, 836−838.
(26) Demadis, K. D.; Katarachia, S. D. *Phosphorus, Sulfur, Silicon* **2004**, *179*, 627−648.
(27) Martinez-Tapia, H. S.; Cabeza, A.; Bruque, S.; Pertierra, P.; Garcia-Granda, S.; Aranda, M. A. G. *J. Solid State Chem.* **2000**, *151*, 122−129.
(28) *Data Collection: SMART-NT Software Reference Manual*, version 5.0; Bruker AXS, Inc.: Madison, WI, 1998.
(29) *Data Reduction: SAINT-NT Software Reference Manual*, version 4.0; Bruker AXS, Inc.: Madison, WI, 1996.
(30) Sheldrick, G. M. *SADABS*, version 2.03; University of Göttingen: Göttingen, Germany, 2002. Sheldrick, G. M. *TWINABS*, version 1.02; University of Göttingen, Göttingen, Germany, 2002.
(31) *WINMAS*, version 940108; Bruker-Franzen Analytik GmbH: Bremen, Germany, 1994,
(32) Herzfeld, J.; Berger, A. E. *J. Chem. Phys.* **1980**, *73*, 6021−6030.
(33) (a) Mehring, M. High Resolution NMR Spectroscopy in Solids. In *NMR - Basic Principles and Progress*; Vol. 11, Diehl, P., Fluck, E., Kosfeld, R., Eds.; Springer-Verlag: Berlin, 1976. (b) Mason, J. *Solid State NMR* **1993**, *2*, 285−288. (c) Harris, R. K.; Becker, E. D.; Cabral De Menezes, S. M.; Granger, P.; Hoffman, R. E.; Zilm, K. W. *Solid State NMR* **2008**, *33*, 41−56.
(34) (a) Kresse, G.; Furthmüller, J. *Phys. Rev.* **1996**, *B 54*, 11169−11186. (b) Kresse, G.; Furthmüller, J. *Comput. Mater. Sci.* **1996**, *6*, 15−50. (c) Kresse, G.; Hafner, J. *Phys. Rev. B* **1993**, *47*, 558−561. (d) Kresse, G.; Hafner, J. *Phys. Rev. B* **1994**, *49*, 14251−14269.
(35) (a) Perdew, J. P.; Chevary, J. A.; Vosko, S. H.; Jackson, K. A.; Pederson, M. R.; Singh, D. J.; Fiolhais, C. *Phys. Rev. B* **1992**, *46*, 6671−6687. (b) Perdew, J. P.; Chevary, J. A.; Vosko, S. H.; Jackson, K. A.; Pederson, M. R.; Singh, D. J.; Fiolhais, C. *Phys. Rev. B* **1993**, *48*, 4978.
(36) (a) Blöchl, P. E. *Phys. Rev. B* **1994**, *50*, 17953−17979. (b) Kresse, G.; Joubert, D. *Phys. Rev. B* **1999**, *59*, 1758−1775.
(37) Monkhorst, H. J.; Pack, J. D. *Phys. Rev. B* **1976**, *13*, 5188−5192.

(38) Blöchl, P. E.; Jepsen, O.; Andersen, O. K. *Phys. Rev. B* **1994**, *49*, 16223−16233.
(39) Stueber, D. *Concepts Magn. Reson. A* **2006**, *28*, 347−368.
(40) (a) Krishnan, R.; Binkley, J.; Seeger, R.; Pople, J. *J. Chem. Phys.* **1980**, *72*, 650−654. (b) McLean, A. D.; Chandler, G. S. *J. Chem. Phys.* **1980**, *72*, 5639−5648. (c) Blaudeau, J.; McGrath, M. P.; Curtiss, L. A.; Radom, L. *J. Chem. Phys.* **1997**, *107*, 5016−5021.
(41) (a) Hariharan, P. C.; Pople, J. A. *Theor. Chim. Acta* **1973**, *28*, 213−222. (b) Francl, M. M.; Petro, W. J.; Hehre, W. J.; Binkley, J. S.; Gordon, M. S.; DeFrees, D. J.; Pople, J. A. *J. Chem. Phys.* **1982**, *77*, 3654−3665. (c) Rassolov, V.; Pople, J. A.; Ratner, M.; Windus, T. *J. Chem. Phys.* **1998**, *109*, 1223−1129.
(42) Stevens, W. J.; Basch, H.; Krauss, M. *J. Chem. Phys.* **1984**, *81*, 6026−6033.
(43) Frisch, M. J.; et al. *Gaussian 03*, revision D01; 2004. Full reference given in the Supporting Information.
(44) Adamo, C.; Barone, V. *J. Chem. Phys.* **1998**, *108*, 664−675.
(45) Glendering, E. D.; Badenhoop, J. K.; Reed, A. E.; Carpenter, J. E.; Bohmann, J. A.; Morales, C. M.; Weinhold, F. *NBO 5.0*; Theoretical Chemistry Institute, University of Wisconsin: Madison, WI, 2001.
(46) Wolinski, K.; Hinton, J. F.; Pulay, P. *J. Am. Chem. Soc.* **1990**, *112*, 8251−8265.
(47) The relation between δ_s and σ_s is given according to the IUPAC definitions by (i) $\delta_s = (\nu_s - \nu_{ref})/\nu_{ref}$ and (ii) $\nu_j = (\gamma/2\pi)B_0(1 - \sigma_j)$, where j={s, ref} is the index for the sample or reference, respectively. Inserting ii into i leads to $\delta_s = -(\sigma_s - \sigma_{ref})/(1 - \sigma_{ref}) \approx (\sigma_s - \sigma_{ref})/-1$. Hence, for the calculation of chemical shifts, it would be sufficient to calculate the absolute magnetic shieldings of the sample and reference compounds. Unfortunately, not all reference compounds are easy to treat computationally; e.g., 85% H_3PO_4 is liquid and would require molecular dynamic simulations for a proper treatment. Also, in order to avoid referencing to a single compound, which may be described in a particularly good or bad way by the chosen quantum-chemical model, one frequently prefers to derive the conversion equation by determining fit parameters A and B from a set of experimentally and computationally investigated compounds: $\delta_{s,exp} = (\sigma_{s,calc} - A)/B$. From comparison of the upper two equations, it is obvious that $A = \sigma_{ref}$ and $B = \sigma_{ref} - 1 \approx -1$. As discussed earlier by Kutzelnigg et al.,[48] one may or may not impose the constraint $B = -1$ on the fit. In numerous investigations with unconstrained B, we always found that B was slightly smaller than −1.0 for the chosen mPW1PW model and various basis sets (see the SI of ref 20), so we decided to keep it unconstrained. The deviation of B from −1 may be regarded as an additional fitting parameter to compensate for systematic errors of the calculation.
(48) Kutzelnigg, W.; Fleischer, U.; Schindler, M. The IGLO-Method: Ab-initio Calculation and Interpretation of NMR Chemical Shifts and Magnetic Susceptibilities. In *NMR—Basic Principles and Progress*; Diehl, P., Fluck, E., Günther, H., Kosfeld, R., Seelig, J., Eds.; Springer: Berlin, 1991; Vol. *23*, pp 165−262.
(49) Sharma, C. V. K.; Clearfield, A.; Cabeza, A.; Aranda, M. A. G.; Bruque, S. *J. Am. Chem. Soc.* **2001**, *123*, 2885−2886.
(50) (a) Bauer, S.; Müller, H.; Bein, T.; Stock, N. *Inorg. Chem.* **2005**, *44*, 9464−9470. (b) Demadis, K. D.; Barouda, E.; Raptis, R. G.; Zhao, H. *Inorg. Chem.* **2009**, *48*, 819−821. (c) Demadis, K. D.; Papadaki, M.; Raptis, R. G.; Zhao, H. *J. Solid State Chem.* **2008**, *181*, 679−683. (d) Demadis, K. D.; Papadaki, M.; Raptis, R. G.; Zhao, H. *Chem. Mater.* **2008**, *20*, 4835−4846. (e) Demadis, K. D.; Stavgianoudaki, N. In *Metal Phosphonate Chemistry: From Synthesis to Applications*; Royal Society of Chemistry: London, 2012; Chapter 14.
(51) (a) Grimmer, A.-R. *Spectrochim. Acta* **1978**, *34A*, 941. (b) Dutasta, J. P.; Robert, J. B.; Wiesenfeld, L. *Chem. Phys. Lett.* **1981**, *77*, 336−338. (c) Turner, G. I.; Smith, K. A.; Kirkpatrick, R. J.; Oldfield, E. *J. Magn. Reson.* **1986**, *70*, 408−415. (d) Cheetham, A. K.; Clayden, N. J.; Dobson, C. M.; Jakeman, R. J. *J. Chem. Soc., Chem. Commun.* **1986**, 195−197. (e) Aime, S.; Digilio, G.; Gobetto, R.; Bigi, A.; Ripamonti, A.; Roveri, N.; Gazzano, M. *Inorg. Chem.* **1996**, *35*, 149−154.
(52) (a) Van de Streek, J.; Neumann, M. A. *Acta Crystallogr., Sect. B* **2010**, *66*, 544−558. (b) Mitchell-Koch, K. R.; Matzger, A. J. *J. Pharm. Sci.* **2008**, *97*, 2121−2129. (c) Neumann, M. A.; Perrin, M.-A. *J. Phys. Chem. B* **2005**, *109*, 15531−15541.
(53) Hahn, T., Ed. *International Tables for Crystallography*; Springer: Berlin, 2005; Vol. *A*.
(54) Radeglia, R. *Solid State NMR* **1995**, *4*, 317−321.
(55) (a) Hansen, A. E.; Bouman, T. D. *J. Chem. Phys.* **1989**, *91*, 3552−3560. (b) Hansen, A. E.; Mikkelsen, K. V.; Bak, K. L. *Magn. Reson. Rev.* **1997**, 133−162.
(56) The ovaloid representation is preferable to the more frequently used "ellipsoid representation". It was first introduced by Hansen and Bouman[55] and labeled as "response graphs" at that time. The surface of the ovaloid is a representation of the totality of shielding values $\sigma_{zz}(\theta,\varphi)$ felt by a nucleus at all directions of an external magnetic field: $\sigma_{zz}(\theta,\varphi) = \sigma_{11} \sin^2 \theta \cos^2 \varphi + \sigma_{22} \sin^2 \theta \sin^2 \varphi + \sigma_{33} \cos^2 \theta$. The distance from the center of the ovaloid (the P nuclear site) to any point at its surface is proportional to the shielding of an external magnetic field in that direction. If the magnetic field direction coincides with the positive and negative directions of $\mathbf{e}_1^{PAS}$, $\mathbf{e}_2^{PAS}$, or $\mathbf{e}_3^{PAS}$, the magnetic shielding corresponds to the principal axis values σ_{11}, σ_{22}, and σ_{33}, respectively.
(57) This insight explains also the experimental finding of a correlation between σ_{33} (or δ_{33}) and the average atomic distance $\overline{d}(Pi{-}O_t)$ shown in Figure 4. According to Biot-Savart's law, there is an r^{-2} dependency for the magnetic shielding contributions of volume elements at distance r from the nucleus (see SI of ref 20 for further details). If $d(P{-}O_t)$ increases, the circular currents in that unit take place at a larger distance from the P nucleus; hence, the magnetic shielding σ_{33} decreases and the chemical shift δ_{33} increases. Of course, the same holds for $d(P{-}O_{t'})$, and because $d(P{-}O_t) \approx d(P{-}O_{t'})$ (C_s pseudosymmetry!) it is useful to plot the averaged $\overline{d}(Pi{-}O_t)$ versus δ_{33}.
(58) Schmidt-Rohr, K.; Spiess, H. W. *Multidimensional Solid-State NMR and Polymers*, 3rd ed.; Academic Press: New York, 1999; Appendix B, p 444 ff.